

Large second-order nonlinearity in asymmetric metallic quantum wells

Cite as: Appl. Phys. Lett. **116**, 241105 (2020); <https://doi.org/10.1063/5.0004509>

Submitted: 12 February 2020 . Accepted: 03 June 2020 . Published Online: 16 June 2020

Steven Edward Bopp , Haoliang Qian , Shilong Li, and Zhaowei Liu 



View Online



Export Citation



CrossMark

ARTICLES YOU MAY BE INTERESTED IN

[All-fiber focused beam generator integrated on an optical fiber tip](#)

Applied Physics Letters **116**, 241102 (2020); <https://doi.org/10.1063/5.0007022>

[Terahertz quantum-cascade patch-antenna VECSEL with low power dissipation](#)

Applied Physics Letters **116**, 241103 (2020); <https://doi.org/10.1063/5.0008867>

[Thin plate compression of a sub-petawatt Ti:Sa laser pulses](#)

Applied Physics Letters **116**, 241101 (2020); <https://doi.org/10.1063/5.0008544>

Lock-in Amplifiers
up to 600 MHz



Watch



Large second-order nonlinearity in asymmetric metallic quantum wells

Cite as: Appl. Phys. Lett. **116**, 241105 (2020); doi: [10.1063/5.0004509](https://doi.org/10.1063/5.0004509)

Submitted: 12 February 2020 · Accepted: 3 June 2020 ·

Published Online: 16 June 2020



View Online



Export Citation



CrossMark

Steven Edward Bopp,¹  Haoliang Qian,²  Shilong Li,² and Zhaowei Liu^{1,2,a)} 

AFFILIATIONS

¹Materials Science and Engineering Program, University of California, San Diego, 9500 Gilman Drive, La Jolla, California 92093, USA

²Department of Electrical and Computer Engineering, University of California, San Diego, 9500 Gilman Drive, La Jolla, California 92093, USA

^{a)} Author to whom correspondence should be addressed: zhaowei@ucsd.edu

ABSTRACT

Investigation of new plasmonic material platforms with large optical nonlinearity is crucial for the continued development of nonlinear optics and its applications. Here, we report an enhanced second-order nonlinear effect in metallic quantum wells (QWs), where the intersubband transition plays a dominant role. Centrosymmetry in these metallic QWs is broken by forming multilayers with chemically and structurally distinct barrier oxides above and below a metal nanofilm. For Au-based QWs, we show that a large $\chi^{(2)}$ around 229.6 pm/V in the near infrared was achieved in an asymmetric metallic QW of SiO₂|Au|HfO₂ on a fused silica substrate.

Published under license by AIP Publishing. <https://doi.org/10.1063/5.0004509>

Plasmonics, over the last two decades, has brought unprecedented opportunities to control light at spatial scales previously thought impossible.^{1–4} Extreme optical confinement and enhanced electric fields have allowed plasmonics to offer useful applications ranging from integrated optical circuits^{5–7} to high-performance bio-sensing systems.^{8,9} Recently, these strong optical field enhancements have garnered considerable attention for plasmonics in nonlinear optics¹⁰ and various nonlinear optical processes. Specifically, second and third harmonic generation (SHG/THG) have been realized with low-intensity laser oscillators without costly power amplifiers.^{11–13} However, plasmon-enhanced nonlinear responses are, even in low loss metals like Au and Ag, still very weak for practical applications and limited by the intrinsically small nonlinear susceptibilities of common plasmonic metals.

Recent efforts in the development of quantum-sized metal films on dielectric substrates have greatly enhanced the intrinsic nonlinear susceptibilities of plasmonic materials. Specifically, ultrathin 3-nm Au films show an extraordinarily high optical Kerr susceptibility, four orders of magnitude larger than that of bulk Au.¹⁴ A large dipole momentum associated with the quantum-engineered electronic intersubband transitions in the metallic quantum well (QW) heterostructure as well as extremely large electron concentrations in metallic layers contribute to this effect. Furthermore, intersubband engineering regarding the coupling of TiN-based metallic QW pairs¹⁵ has given a record high second-order susceptibility $\chi^{(2)}$ in the visible to

near-infrared (NIR) spectral range. However, Au and Ag still surpass TiN in the way of technologically relevant plasmonic properties in this frequency range.¹⁶ Therefore, the challenge of realizing a large second-order nonlinearity in the commonly used plasmonic metals Au and Ag to develop further improvements in the field of nonlinear plasmonics still remains.

In this Letter, we demonstrate, as measured by SHG, a record high $\chi^{(2)}$ around 229.6 pm/V at a wavelength of 940 nm in an asymmetric Au metallic QW. Our approach is to confine Au layers via heterostructuring between insulator pairs of varying asymmetry in order to fabricate ultrathin nanocomposites having high $\chi^{(2)}$. Plasmonic materials with such high $\chi^{(2)}$ are expected to enable useful nonlinear effects for various on-chip applications.

A quantum electrostatic model for nanoscale metal films^{14,17–19} was used to estimate the eigenstates and the associated wavefunctions of electrons in three Au QW films with differing increments of structural and chemical asymmetry [Figs. 1(a)–1(c)]. Nine quantized energy states are supported by these asymmetric QWs; the transitions between the seventh and eighth energy states approximately targeted a wavelength of 940 nm.

The $\chi^{(2)}$ of these asymmetric metallic QWs was calculated with perturbation theory along the growth direction (z -axis) [Eq. (1)]. Here, resonance frequencies ω are real, \mathcal{P}_f is the intrinsic permutation operator, N is the free electron density, ϵ_0 is the vacuum permittivity, \hbar is the reduced Planck constant, μ is the dipole transition moment, and

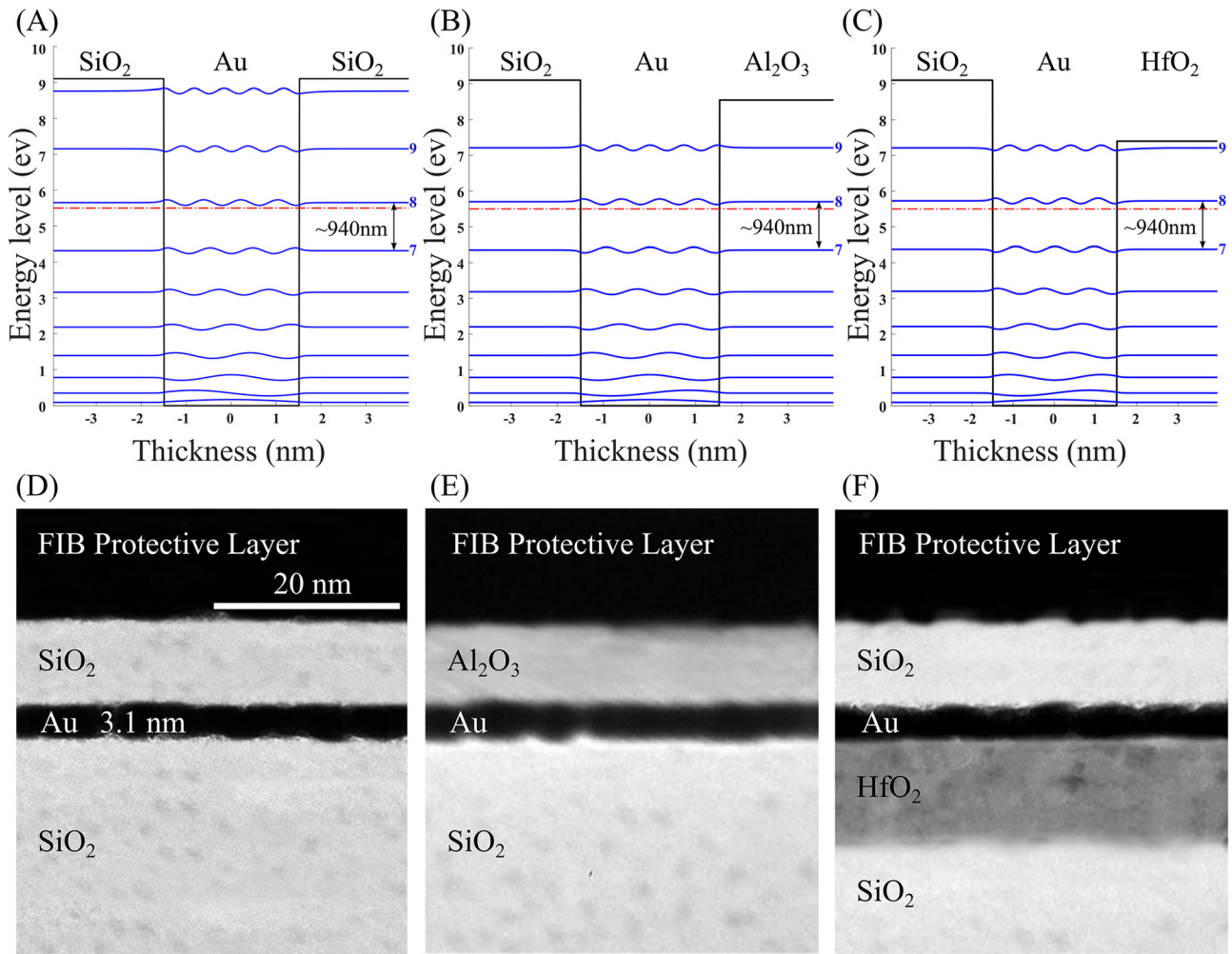


FIG. 1. (a)–(c) Conduction band diagrams corresponding to the below TEM images with wavefunctions (blue solid curves), Fermi energy (red dashes); transition energies and energy states labeled. TEM images of QW devices (d) without, (e) with intermediate, and (f) with maximal structural and chemical asymmetry between barrier layers.

m , n , and g are energy states.²⁰ Most importantly, the term μ_{gn} , and thus $\chi^{(2)}$, only becomes nonzero when the QW barrier potential is asymmetric because the dipole transition moment is an integral of an odd function, which is necessarily zero over a symmetric interval. The barrier asymmetries then induce an asymmetric wavefunction making second-order effects possible in the wells. $\chi^{(2)}$ may then be maximized in a variety of ways including having a large N , as is the case in metals, but most importantly by having a large degree of asymmetry in well layers

$$\chi_{zzz}^{(2)}(2\omega, \omega, \omega) = \frac{N}{\epsilon_0 \hbar^2} \mathcal{P}_f \sum_{mn} \frac{\mu_{gn} \mu_{nm} \mu_{mg}}{(\omega_{ng} - 2\omega)(\omega_{mg} - \omega)}. \quad (1)$$

Because it is difficult to visually see the wavefunction asymmetry in these wells, it may be characterized with a figure of merit (FoM) derived from a two-term Fourier series fitting to the wavefunctions in the region centered at ± 1.7 nm from the centers of the Au films. The FoM is calculated by summing the squares of the cosine factors, dividing them by the sum of the squares of both the sine and cosine terms,

and finally multiplying by a prefactor of $(-1)^{n+1}$, where n is the energy level to account for periodicity in absolute displacement from the nearest whole number. The FoM shows a clear decrease for increasing asymmetry of the structures over all energy levels and a marked decrease in the maximally asymmetric well structure as compared with the symmetric and medium asymmetry structures.

In order to realize these structures, three single QW unit devices were fabricated after simulation. A resonance at the wavelength of 940 nm was targeted with three geometries of increasing chemical and structural asymmetry: (1) symmetric which was expected to have zero $\chi^{(2)}$ —Au between SiO₂ barriers [Fig. 1(d)]; (2) intermediate asymmetry—Au between an Al₂O₃ capping layer and a SiO₂ substrate [Fig. 1(e)]; and (3) maximal asymmetry—Au between a SiO₂ capping layer and a substrate coated with HfO₂ [Fig. 1(f)]. All oxide barrier layers are approximately 10 nm thick and well-formed with smooth interfaces, while Au films are similarly smooth and well-formed with an approximate thickness of 3.1 nm.

Nanofilms of Au were sputtered with an AJA Orion DC sputter system with a target power of 50 W in a 5 mTorr Ar atmosphere with a 5 sccm flow rate at standard temperature. SiO₂ insulators were sputtered using an AJA Orion 8 UHV RF sputter system with a target power of 150 W in a 5 mTorr Ar atmosphere with a 5 sccm flow rate at standard temperature; Al₂O₃ insulators were grown in the same system at 150 W in the same condition of a 5 mTorr Ar atmosphere with a 5 sccm flow rate at standard temperature. HfO₂ nanofilms were fabricated in a Beneq TFS200 atomic layer deposition system from precursors tetrakis(dimethylamido)hafnium(IV) (TDMAH), and de-ionized water at 200 °C. Nanofilms were imaged with transmission electron microscopy (TEM) in a FEI Spirit system [Figs. 1(d)–1(f)] on samples prepared via the focused ion beam (FIB) lift out method with a Pt protection layer.

$\chi^{(2)}$ in a real material may be determined by measurement of a second-order nonlinear process, such as SHG.²¹ For a sufficient optical density to excite the SHG,^{22–24} illumination from a MaiTai 100 fs pulsed laser system with an 80 MHz repetition rate and 10 mW incident average power was used. A (Vega) power meter was used to measure pulse power, and SHG emission was collected by a [Horiba picosecond photon detector (PPD)] photon counting detector. 45° incidence p-polarized pulsed light was focused onto the sample with a spot size of 2 μm, and the reflected light wave was collected with a 50× objective (NA = 0.8) in an Olympus IX81 microscope. Incident light was ported through a dichroic prism into the objective where it was focused onto the sample and recollected whereupon emission light was passed through the prism, and through an excitation filter for downstream measurement.

To assess the performance of these devices, SHG spectra (e.g., fraction of counts corresponding to the doubled frequency) were collected by scanning the sample's emission wavelengths from 490 to 510 nm [Fig. 2(a)] under illumination with a fixed incident fundamental wavelength centered at 1000 nm having a full width at half the maximum bandwidth of 8.83 nm. The pump laser linewidth is approximately as broad as the signal linewidth. The metallic QW will not only have high $\chi^{(2)}$ but high $\chi^{(3)}$ as well, a result of the instantaneous Kerr effect which contributes broadening¹⁴ that can be seen in the clearly visible spectral wings present in the spectrum. The inset of Fig. 2(a) shows the SHG spot at the image plane as collected via a High-Sensitivity CMOS Camera (ThorLabs DCC1240C). The spectrum shows a strong, sharp peak at the doubled frequency.

To calibrate our system, a β-BaB₂O₄ (BBO) crystal which has known $\chi^{(2)}$ is placed in the free space beamline ahead of the microscope and the second harmonic signal generated by the BBO crystal is sent through a monochromator into the PPD. Power dependence of the SHG signal intensity (i.e., incident power vs photon counts) for the maximally asymmetric SiO₂|Au|HfO₂ QW was measured using the IX81 microscope and a photon counting detector in order to separate the contributions of second- and third-order effects to signal; results are shown in Fig. 2(b). The dataset were initially fit to a single term power function ax^b showing $b = 2.664$. This value of the b parameter deviates from the expected value of $b = 2$, which would be the ideal case for a purely SHG signal. Instead, the b parameter here indicated a combination of some fraction SHG and likely a third-order multiphoton event. Figure 2(b) shows the power dependence of signal fitted to a sum of power functions of the form $ax^2 + bx^3$ with factors $a = 6.458$, and $b = 1.26$ indicating that 83.67% of the total signal intensity resulted from SHG.

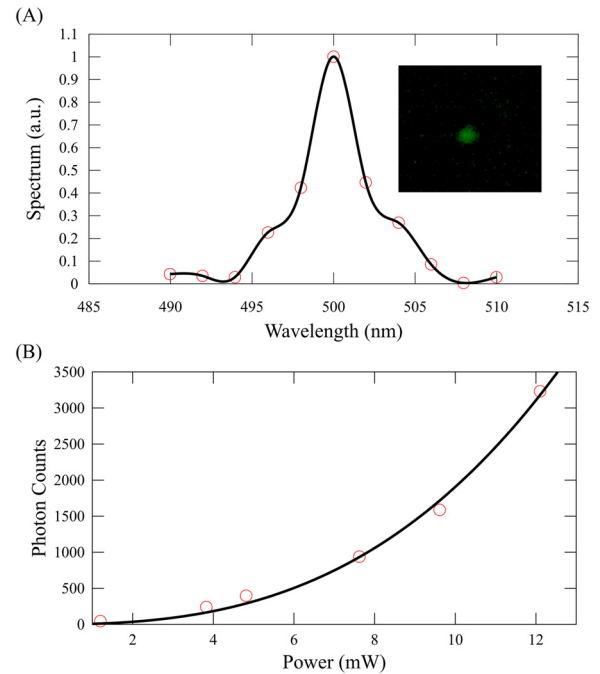


FIG. 2. (a) Spectrum as a function of wavelength centered at the double transition of 500 nm from the 1000 nm fundamental excitation. Inset: long exposure micrograph at the image plane of the frequency-doubled signal. (b) Power-dependent SHG signal from the maximally asymmetric QW: photon counts show a mixture of second- and third-order dependence fitted to $6.458x^2 + 1.26x^3$.

Figure 3(a) tabulates the increase in peak emission power with respect to increasing structural asymmetry normalized to the SiO₂|Au|HfO₂ QW for all devices tested. The symmetric case shows a nearly complete emission extinction. Experimentally, $|\chi^{(2)}|$ was measured by relation to photon counts from the detector as calibrated with the BBO crystal. Wavelength-dependent $|\chi^{(2)}|$ was then calculated based on measurements according to Eq. (2), where $I_{2\omega}$ and I_{ω} are the peak SHG intensity and the peak excitation pulse intensity, respectively; $n_{2\omega}$ and n_{ω} are the refractive indices of the nonlinear medium at the doubled and fundamental frequencies, respectively. c is the speed of light in vacuum, ϵ_0 is the vacuum permittivity, ω is the angular frequency of the excitation, and l is the interaction length of the nonlinear medium¹⁵

$$\chi^{(2)} = \sqrt{\frac{2I_{2\omega}n_{2\omega}n_{\omega}^2\epsilon^3\epsilon_0}{I_{\omega}^2\omega^2l^2}}. \quad (2)$$

Measurement and simulation of effective wavelength-dependent $|\chi^{(2)}|$ for the SiO₂|Au|HfO₂ QW are plotted in Fig. 3(b). The spectrum exhibits a clear, sharp peak at the doubled frequency. Since $\chi^{(2)} \propto \sqrt{I_{2\omega}}$, values are scaled 91.47% (according to the root of the intensity calculated earlier) along the $\chi^{(2)}$ axis to exclude third-order contributions to the peak SHG emission power. The maximum measured intensity of the SiO₂|Au|HfO₂ QW is 229.6 pm/V, and our simulation¹⁸ fits well with the dataset.

We have realized a large $\chi^{(2)}$, calculated from the efficiency of SHG in Au-based QWs, relying on electronic intersubband transitions. Our asymmetric metallic QWs show that $\chi^{(2)}$ increases with

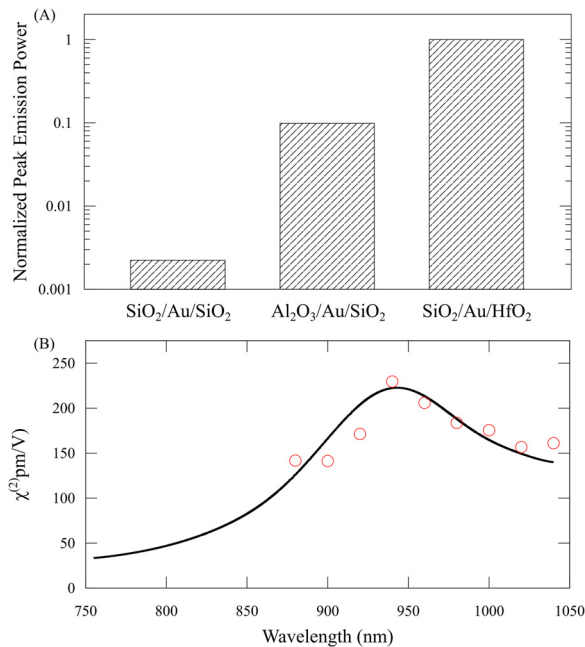


FIG. 3. (a) Normalized peak emission power for the three QW devices of increasing chemical and structural asymmetry, showing correspondingly increasing emission power. (b) Magnitude of $\chi^{(2)}$ as a function of wavelength for the maximally asymmetric $\text{SiO}_2|\text{Au}|\text{HfO}_2$ QW, showing a maximum measured $\chi^{(2)}$ magnitude of 229.6 pm/V at 940 nm. Red circles indicate measurements, and the black curve indicates simulation.

decreasing symmetry, and we demonstrate a large $\chi^{(2)}$ around 229.6 pm/V in the NIR at a wavelength of approximately 940 nm for our maximally asymmetric QW. Increased susceptibility such as shown here allows for enhanced efficiency of nonlinear processes. Plasmonic materials with high $\chi^{(2)}$ allow for control of light within miniature and flat photonic devices with external light and/or electric fields. Future directions for this research include chip-scale integration of nonlinear optical devices with improved efficiency, broadband nonlinear effects from heterostructuring, and various plasmonic enhancements for nonlinear effects in these devices.

This work was supported by the DARPA DSO-NLM Program (Grant No. HR00111820038). Steven Edward Bopp thanks the support of the Department of Defense (DoD) through the National Defense Science & Engineering Graduate (NDSEG) Fellowship Program.

DATA AVAILABILITY

The data that support the findings of this study are available from the corresponding author upon reasonable request.

REFERENCES

- ¹E. Ozbay, *Science* **311**, 189 (2006).
- ²S. Kawata, Y. Inouye, and P. Verma, *Nat. Photonics* **3**, 388 (2009).
- ³J. A. Schuller, E. S. Barnard, W. Cai, Y. C. Jun, J. S. White, and M. L. Brongersma, *Nat. Mater.* **9**, 193 (2010).
- ⁴Z. V. Vardeny, A. Nahata, and A. Agrawal, *Nat. Photonics* **7**, 177 (2013).
- ⁵N. Engheta, *Science* **317**, 1698 (2007).
- ⁶Y. Sun, B. Edwards, A. Alù, and N. Engheta, *Nat. Mater.* **11**, 208 (2012).
- ⁷D. E. Chang, V. Vuletić, and M. D. Lukin, *Nat. Photonics* **8**, 685 (2014).
- ⁸J. N. Anker, W. P. Hall, O. Lyandres, N. C. Shah, J. Zhao, and R. P. Van Duyne, *Nat. Mater.* **7**, 442 (2008).
- ⁹A. G. Brolo, *Nat. Photonics* **6**, 709 (2012).
- ¹⁰M. Kauranen and A. V. Zayats, *Nat. Photonics* **6**, 737 (2012).
- ¹¹W. Cai, A. P. Vasudev, and M. L. Brongersma, *Science* **333**, 1720 (2011).
- ¹²S. Kim, J. Jin, Y. Kim, I. Park, Y. Kim, and S. Kim, *Nature* **453**, 757 (2008).
- ¹³T. Hanke, G. Krauss, D. Träutlein, B. Wild, R. Bratschitsch, and A. Leitenstorfer, *Phys. Rev. Lett.* **103**(1), 257404 (2009).
- ¹⁴H. Qian, Y. Xiao, and Z. Liu, *Nat. Commun.* **7**, 13153 (2016).
- ¹⁵H. Qian, S. Li, C.-F. Chen, S.-W. Hsu, S. E. Bopp, Q. Ma, A. R. Tao, and Z. Liu, *Light: Sci. Appl.* **8**, 13 (2019).
- ¹⁶U. Guler, A. Boltasseva, and V. M. Shalaev, *Science* **344**, 263 (2014).
- ¹⁷A. Gabbay, J. Reno, J. R. Wendt, A. Gin, M. C. Wanke, M. B. Sinclair, E. Shaner, and I. Brener, *Appl. Phys. Lett.* **98**, 203103 (2011).
- ¹⁸H. Qian, Y. Xiao, D. Lepage, L. Chen, and Z. Liu, *Nanophotonics* **4**, 413 (2015).
- ¹⁹C. Weisbuch and V. Borge, *Quantum Semiconductor Structures*, 1st ed. (Academic Press, New York, 1991).
- ²⁰R. W. Boyd, *Nonlinear Optics*, 3rd ed. (Academic Press, 2008).
- ²¹R. Menzel, *Photonics Linear and Nonlinear Interactions of Laser Light and Matter*, 1st ed. (Springer, 2001).
- ²²C. Gmachl, O. Mails, and B. Alexey, *Intersubband Transitions in Quantum Structures*, 1st ed. (McGraw-Hill, New York, 2010).
- ²³R. Dalven, *Introduction to Applied Solid State Physics*, 2nd ed. (Plenum Press, New York, 1990).
- ²⁴J. F. McGilp, *J. Phys. D* **29**, 1812 (1996).